A Density Functional Theory Insight into Structural, Mechanical, and Optical Properties of Rb_2LiTlF_6 Double Perovskite

Elkana K. Rugut,* Nnditshedzeni E. Maluta, Regina R. Maphanga, Refilwe E. Mapasha, and Joseph K. Kirui

The density functional theory (DFT) is applied to systematically investigate the geometrical structure, electronic, mechanical, vibrational, and optical properties of double perovskite Rb_2LiTlF_6 in its cubic phase. To the best of one's knowledge, many physical properties of this compound are still not well established or not yet investigated; such as phonon properties, mechanical behavior, thermal properties, and so on. In this work, the stability of Rb_2LiTlF_6 is explored by looking at its thermodynamical behavior through calculation of formation energy, cohesive energy, Goldschmidt tolerance factor, and phonon dispersion. Its mechanical properties are examined based on various characterization descriptors such as the independent elastic coefficients, bulk, shear, and Young's modulus, ratios such as Pugh and Poisson's, Kleinnman parameter, Zener anisotropy factor, Debye temperature, and melting temperature. Sound velocity in this material is predicted from the values of the bulk and shear modulus obtained. Thermal expansion coefficient at finite temperatures are obtained using the approach of quasi-harmonic approximation. Its electronic property is also investigated using generalized gradient approximation and also hybrid functionals. At a later stage, its optical behavior upon the effect of light excitation is explored using the many body pertubation theory approximation. Having envisioned this material as a wide band gap semiconductor, it can be useful in numerous applications such as designing the top-cell of tandem photovoltaic configuration, photodetection, and light emitting diodes. It is strongly believed that this work will provide a helpful guidance for future experimental and theoretical investigations of this material.

1. Introduction

Among the single perovskites, methyl-ammonium lead iodide ($MAPbI_3$) has been extensively explored as a promising solar cell absorber due to its unusual combination of a distinctive photo-physical and electronic properties[1–4] that give rise to a high power conversion efficiency.[5] However, it has some shortcomings such as toxicity due to the presence of lead (Pb) and instability when exposed to moisture[6] and heat,[7,8] which pose a significant hurdle to its extensive applications. Moreover, there is a strong structural framework similarity between the double and the single perovskites since the latter are derived from the former. The double perovskite structure allows incorporation of diversified range of cations into the octahedrally coordinated B/B' site.[9] This open a plethora of electronic and compositional structure tuning that can lead to varying fundamental properties geared toward determining a potential substitute to $MAPbI_3$ as a solar absorber.

Contrary to the single perovskites in which massive progressive research has been carried out, double perovskites have not been extensively studied, which open a window for exploration. In our compound of interest, the cations alternate in all

E. K. Rugut, N. E. Maluta, J. K. Kirui
Department of Physics
University of Venda
Thohoyandou, South Africa
E-mail: elkana.rugut@univen.ac.za

The ORCID identification number(s) for the author(s) of this article can be found under https://doi.org/10.1002/adem.202300995.

N. E. Maluta, R. R. Maphanga, R. E. Mapasha, J. K. Kirui
National Institute for Theoretical and Computational Sciences (NITheCS)
Stellenbosch, South Africa

R. R. Maphanga
Next Generation Enterprises and Institutions Cluster
Council for Scientific and Industrial Research
Pretoria, South Africa

R. E. Mapasha
Department of Physics
University of Pretoria
Pretoria, South Africa

three dimensions creating a rock-salt-type of arrangement that is also known as the elpasolite structure, similar to the mineral elpasolite (K_2NaAlF_6). Normally, the so-called elpasolites represent a huge group of compounds not only halides but also oxides, sulfides, nitrates, and cyanides as discussed therein.[10] Our elpasolite halide of interest possesses the chemical formula $A_2^+B^+B'^{3+}X_6^-$, where A^+ and B^+ are alkali metal cations, B'^{3+} is a trivalent cation belonging to post-transition metals and X^- is a halogen anion.

Partial cation substitution in an ideal perovskite structure ABX_3 is a common technique of tailoring the properties of perovskite compounds. This substitution can occur at either A or B site in varying degrees. However, in recent years there has been a particular interest in the case where exactly half of the B-site cation is substituted with another cation giving rise to $A_2BB'X_6$ double perovskites that possess fascinating features.[11] In 2016, Slavney et al.[12] carried out experimental studies on $Cs_2AgBiBr_6$ double perovskite, from which they realized that the material had inherently high defect tolerance, having an indirect band gap of 1.95 eV, that is suitable for solar cell applications. This motivated further exploration of both inorganic and hybrid halide double perovskites for photovoltaic and other optoelectronic applications. Other elpasolite structures that have been successfully synthesized include $Cs_2AgInCl_6$,[13] Cs_2AgTlX_6 (X = Cl, Br)[14] and $Cs_2AgSbCl_6$,[15] just to mention a few.

Recently, Wu et al.[16] have synthesized $Ba_xSr_{2-x}FeVO_6$ ($x = 0.0$–2.0) double perovskite ceramics via the solid-state reaction method, whereby they found out that the stated ceramics exhibit a strong frequency-dependent dielectric behavior. Moreover, Xiang et al.[17] proposed novel double perovskite $Ca_2Gd_{0.5}Nb_{1-x}W_{5x/6}O_6:0.5Eu^{3+}$ phosphors that possessed excellent thermal stability and high color purity for white light-emitting diodes (LEDs). Hossain et al.[18] carried out the photovoltaic performance enhancement of Cs_2BiAgI_6 double perovskite by optimizing the optoelectronic parameters of the absorber, electron transport layer, hole transport layer, and various interface layers in which the highest power conversion efficiency was recorded to be 23.71%.

Manzoor et al. have examined the transport and optoelectronic properties of double perovskites Rb_2LiTlX_6 (X = Cl, Br) through a density functional theory (DFT) approach as potential candidates for thermoelectric and solar cell applications.[19] The compounds explored by Manzoor et al. are analogous to the one reported in this work, the only difference is the halogen element considered that is chlorine and bromine in their case as compared to fluorine in our case. From their findings, $Rb_2LiTlCl_6$ and $Rb_2LiTlBr_6$ absorb light within the visible range of the electromagnetic spectrum with direct band gaps at Γ-point. Little information is provided in materials project database[20] about our quaternary compound of interest (Rb_2LiTlF_6) such as its predicted ground state properties like crystal structure, band gap, lattice constant, density, and formation energy.

This provides the foundation and also act as a yardstick to our study since in-depth examination of the ground state properties together with its optical analysis is yet to be fully explored. Thus, we applied DFT formalism to extensively predict and examine the physical properties of this material by carrying out simulations and later scrutinizing the resultant data so as to envision its properties and possibly suggest its application. The remaining

part of this work is organized as follows; we describe the computational methods applied followed by the results obtained alongside their discussion. At a later stage, we summarize and conclude our research findings and recommend on the possible areas of application.

2. Computational Methods

First-principles calculations were performed using the Vienna abinitio simulation package (VASP),[21] which is a plane-wave all-electron code using the projector-augmented wave method to describe the electron–core interaction for systems with periodic boundary conditions entrenched on the ability of DFT[22] to solve the quantum problem for materials. The generalized gradient approximation[23] with the Perdew–Burke–Ernzehof (PBE) functional and PBEsol which is a flavor of PBE functional that has been revised for solids were used in this study. In principle, PBEsol is a functional that is specifically written to describe the behavior of solids with good accuracy as it minimizes their reliance on error cancellation between the exchange part and the correlation part.[24] For this reason together with absence of the experimental data of this material, with an aim of achieving precise lattice constant representation, we opted to use the PBEsol functional for further calculations such as electronic and phonon dispersion investigation.

To obtain the ground state properties of this compound, the Brillouin zones were sampled using a Monkhorst–Pack k-point mesh of $10 \times 10 \times 10$. The plane-wave expansion was truncated at a cut-off energy of 520 eV, this was arrived at after performing convergence test for its reliability as provided in the supporting information. The static first principles calculations were conducted with a precision of 10^{-6} eV for the total energy difference between two successive self-consistency steps and 10^{-2} (eV Å^{-1}) as the convergence criterion for the forces on atoms. Phonon calculations were done by applying a finite displacement method, employing a $2 \times 2 \times 2$ supercell using the phonopy software.[25] For mechanical studies, we applied a stress–strain approach for calculating elastic constants, whereby after extracting our stiffness matrix, the matrix was analyzed to obtain average properties such as bulk and shear modulus as well as Poisson's ratio among other mechanical properties using elate tensor analysis tool.[26]

The ground state wavefunctions obtained from a hybrid functional (HSE06 with default mixing parameter of 25%) were used as input for optical calculations because of their ability to describe accurately the value of the band gap of materials, which is often underestimated by the standard Kohn–Sham DFT calculations due to the self-correlation error of electrons and the existence of a derivative discontinuity of the energy with respect to the number of electrons.[27] For optical properties, a k-point mesh of $6 \times 6 \times 6$ was applied and the plane wave cut-off energy was adjusted to 300 eV due to the demanding computational nature of the optical calculations as a trade-off.

For the remaining part of this section, we provide a detailed description of how cohesive energy, formation energy, and tolerance factor were computed. Basically, cohesive energy is the amount of energy that must be supplied to a solid to separate its constituents into neutral free atoms at rest and at infinite separation in which the energy calculations for both the product

(compound) and the reactants (constituent atoms) have to be performed at the same level of accuracy in order to attain a precise value of cohesive energy (E_{coh}).[28] Equation (1) indicates how the cohesive energy was computed in this study.

$$E_{coh} = E_{Rb_2LiTlF_6}^{solid} - [2E_{Rb}^{solid} + E_{Li}^{solid} + E_{Tl}^{solid} + 3E_{F_2}^{solid}] \tag{1}$$

where $E_{Rb_2LiTlF_6}^{solid}$ is the total ground-state energy of the quaternary compound while E_{Rb}^{solid}, E_{Li}^{solid}, E_{Tl}^{solid} and $E_{F_2}^{solid}$ are the total energies of the constituent elements; that is rubidium, lithium, thallium, and fluorine, respectively. In contrast, the formation energy is the difference between cohesive energy of product, E_{coh} (product that appears on the right hand side of Equation (2) and cohesive energy of reactants, E_{coh} (reactants that appear on the left hand side of Equation (2)). The chemical reactivity equation of Rb_2LiTlF_6 quaternary compound considered in this study is given by Equation (2) as

$$2Rb(s) + Li(s) + Tl(s) + 3F_2(s) \rightarrow Rb_2LiTlF_6(s) \tag{2}$$
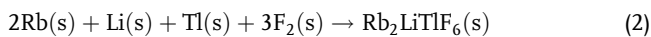
Therefore, the formation energy can then be expressed as

$$E_F = E_{coh}(product) - \sum E_{coh}(reactants) \tag{3}$$

or

$$\begin{aligned} E_F(Rb_2LiTlF_6) \\ &= E_{coh}(Rb_2LiTlF_6) \\ &\quad - \left[\frac{2E_{coh}(Rb) + E_{coh}(Li) + E_{coh}(Tl) + 3E_{coh}(F_2)}{7}\right] \end{aligned} \tag{4}$$

Equation (4) indicates how the cohesive energy was computed in this study. From Equation (1) and (4), negative values of cohesive and formation energies will indicate that the compound is stable against decomposition into its constituent atoms and elemental solids. Based on the negative values of both the formation energy and the cohesive energy obtained in our study as enlisted in Table, we infer that cubic Rb_2LiTlF_6 is thermo-dynamically stable implying that it cannot decompose to its constituent atoms or elemental solids, thus indicating its energetic stabilization.

The Goldschmidt tolerance factor (t_G) of the double perovskite under study was computed using the expression provided in Equation (5)

$$t_G = \frac{(r_{Rb} + r_F)}{\sqrt{2}(r_B + r_F)} \tag{5}$$

where r_{Rb} and r_F are the atomic radii of rubidium and fluorine atoms, respectively. In contrast, r_B is the average of the atomic radii of lithium and thallium atoms. The computed value was obtained to be 0.97, which is within the range of 0.90–1.00 indicating that the double perovskite under study is highly stable.[29] Generally, a compound whose tolerance factor is close to unity ($t_G \approx 1$) is typically predicted to be cubic as it indicates that the A-site cation has the appropriate size to fit in the interstices.[30] In perovskite materials, the tendency to distort from the cubic α-phase has been shown to correlate with the size of the A-site cation relative to the size of the cuboctahedral void in which it resides.[31]

3. Results and Discussion

In this section; we present and discuss the structural, energetic, mechanical, electronic, vibrational, thermal, and optical properties of the quaternary compound of interest.

3.1. Structural Properties of Rb_2LiTlF_6

Figure 1a,b show the face centered cubic crystal structure of Rb_2LiTlF_6, space group Fm-3m in the ball-and-stick and polyhedral format; where the black, green, blue, and red spheres represent rubidium, lithium, thallium, and fluorine atoms, respectively as visualized using vesta tool.[32] By minimizing the total energy with respect to the variation of cell size using both the PBE and PBEsol functionals, we were able to obtain optimized values of the equilibrium lattice constant at the ground state level as supported by the equation of state (EOS) plots supplied in **Figure 2**a,b. This is worth exploring because arrangement of atoms governs the physical properties of material such as electronic, magnetic, and optical characteristics among others. **Table 1** provides the structural parameters such as the optimized lattice constants, predicted density, formation, and cohesive energies per atom as well as the bulk modulus; where we present our results and benchmark with the existing theoretical data. We spot a correlation between our predicted structural data such as that of lattice constant with theoretical data provided in materials project database.[20]

3.2. Mechanical Properties of Rb_2LiTlF_6

The elastic properties are instrumental when elucidating the structural stability and stiffness of materials. Mechanical stability is an important criterion used to gauge if a material can be used in any type of application. Mechanical properties of solid materials are primarily dependent on the elastic constants, which determine the response of the crystal to external forces that subject its atoms to strain or stress. A set of three elastic constants C_{11}, C_{12}, and C_{44} are sufficient to examine the mechanical response of any cubic system. In **Table 2**, we present the numerical values of the three independent elastic coefficients alongside the bulk and shear moduli, Pugh ratio, Young's moduli as well as the Poisson's ratio of the cubic Rb_2LiTlF_6.

To the best of our knowledge, this is the first attempt on its mechanical properties since no experimental or theoretical information about its mechanical behaviour exists so far. The independent elastic coefficients C_{ij}, bulk modulus (B), shear modulus (G), and Young's modulus (E) are given in gigapascals (GPa) and the predicted numerical data of B, G, E, and ν are in accordance with the Hill's averaging scheme,[33] as it is an average of the Voight and Reuss schemes.

The computed values of the independent elastic coefficients provided in Table 2 conform to Born mechanical stability criteria for cubic systems[34] when substituted onto Equation (6), which affirms that cubic Rb_2LiTlF_6 is indeed a mechanically stable material.

$$C_{11} - C_{12} > 0; \quad C_{11} + 2C_{12} > 0; \quad C_{44} > 0 \tag{6}$$

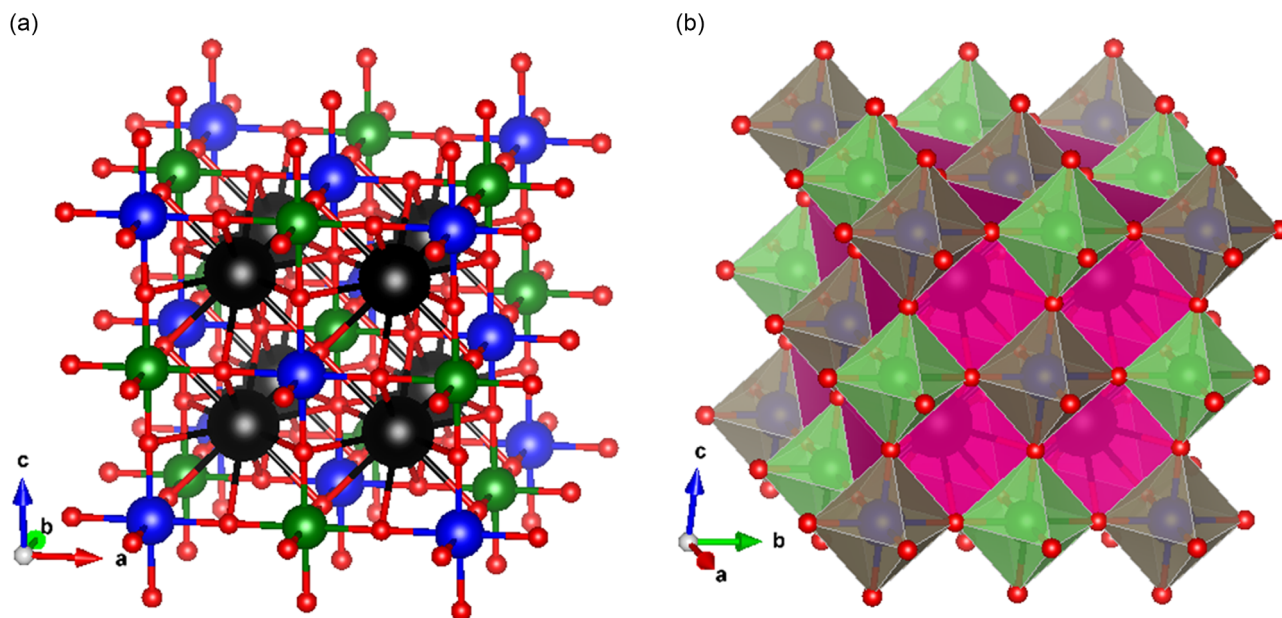Consistency of our prediction is visible when one compares the numerical values of the bulk modulus obtained using two

Figure 1. a) Crystal structure of cubic Rb_2LiTlF_6 in ball-and-stick format, where the black, green, blue, and red spheres represent rubidium, lithium, thallium, and fluorine atoms, respectively; b) Polyhedral representation of the cubic perovskite structure of Rb_2LiTlF_6, indicating its atomic arrangement at various sites.
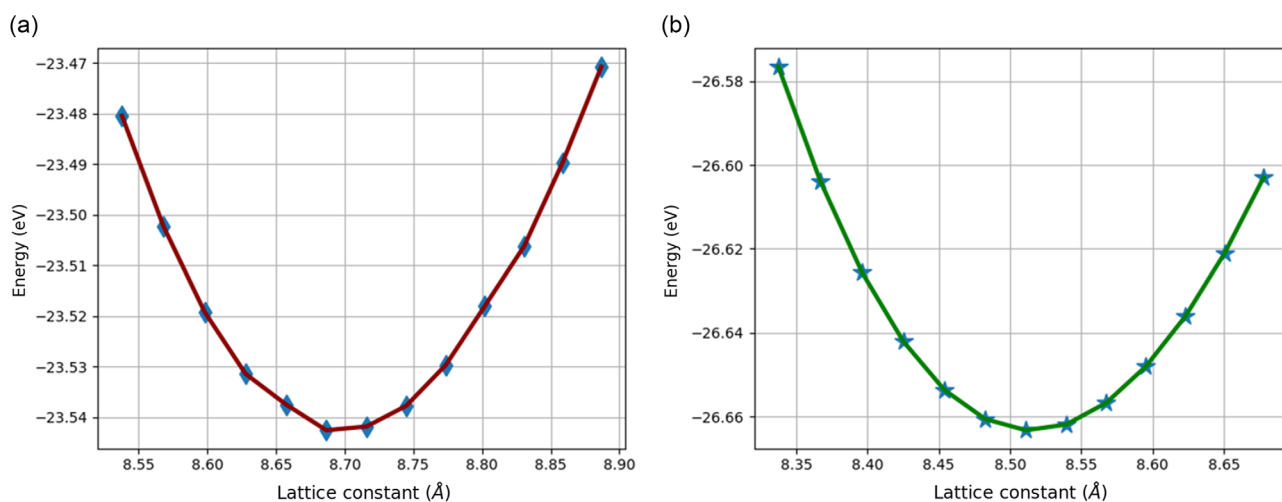

Figure 2. a) Equation of state plot indicating how equilibrium lattice constant was extracted using PBE functional; b) Equation of state plot indicating how equilibrium lattice constant was extracted using PBEsol functional.

Table 1. Structural parameters of cubic Rb_2LiTlF_6 perovskite whereby a, ρ, E_{form}, E_{coh}, and B denote the lattice constant, density, formation energy, cohesive energy, and bulk modulus, respectively.

Functional	a [Å]	ρ [g cm^{-3}]	E_{form} [eV atom^{-1}]	E_{coh} [eV atom^{-1}]	B [GPa]
Others[20] (PBE)	8.690	5.02	−2.73	–	–
Calc. (PBE)	8.687	5.03	−2.46	−3.70	36.30
Calc. (PBEsol)	8.515	5.34	−2.49	−3.90	41.57

Table 2. Mechanical parameters of cubic Rb_2LiTlF_6 perovskite whereby C_{ij}, ν, B, G, and E represents the independent elastic coefficients, Poisson's ratio, bulk, shear, and young's modulus, respectively.

	C_{11}	C_{12}	C_{44}	B	G	B/G	E	ν
Calc. (PBE)	46.921	31.868	22.956	36.886	14.699	2.51	38.926	0.32
Calc. (PBEsol)	60.448	33.171	24.409	42.263	19.325	2.19	50.307	0.30

ADVANCED
SCIENCE NEWS
www.advancedsciencenews.com

ADVANCED
ENGINEERING
MATERIALS
www.aem-journal.com

different approaches that is from the EOS as given in Table 1 and from the elastic constant calculation as enlisted in Table 2, where a deviation of less than 2% was realized. This slight disparity can be attributed to the different assumptions and approximations used in the stated approaches.[35] For instance, in the elastic constant approach, the crystal structure and anisotropy is taken into consideration. This is neglected in the energy–volume relation as it assumes that the material behaves as a continuous medium and considers the change in energy as the system is compressed or expanded. Consequently, this affects the magnitude of the computed bulk modulus.

Generally, the bulk modulus indicates the resistance of a material against volume change under isotropic hydrostatic pressure, hence there exists some correlation between the volume of a material and its bulk modulus such that a larger cell volume may result in a smaller value of bulk modulus. This is noticeable for cubic Rb_2LiTlF_6 in that our predicted value of the equilibrium lattice constant is larger when PBE functional is used relative to PBEsol and the obtained numerical values of bulk modulus are smaller for PBE compared to those obtained using PBEsol as shown in Table 1 and 2.

The shear and bulk modulus together with the Poisson's ratio play decisive roles in evaluating the mechanical properties of any material. Pugh proposed that if the quotient of the bulk to shear modulus (B/G) value is less than the critical value of 1.75,[36] the material is considered brittle, otherwise it is ductile. Bear in mind that ductility and brittleness play a key role during manufacturing of materials.

Moreover, the Poisson's ratio correlates with Pugh's criterion such that if $\nu > 0.26$ the compound is ductile.[37] The values B/G and ν listed in Table 2 indicate that indeed the cubic Rb_2LiTlF_6 is a ductile material, therefore it can withstand large strains and large energy absorption before fracture. Cauchy's pressure value which is basically the difference between C_{12} and C_{44} also serves as an indicator and can be used to ascertain if a material is brittle or ductile, a positive (negative) value of Cauchy's pressure ($C_{12}-C_{44}$) determines the ductile (brittle) nature of the material.[38] For our case, C_{12} exceeds C_{44} for both functionals, hence reinforcing our earlier statement that cubic Rb_2LiTlF_6 is a ductile quaternary compound.

In addition, by establishing the values of the independent elastic constants, one is able to deduce other mechanical properties of a material such as its anisotropy, ductility/brittleness, sound velocity, melting, and Debye temperature among others as briefly discussed below. Zener anisotropy factor denoted by A, is a pointer to the degree of elastic anisotropy in a solid structure. For a completely isotropic material, where the mechanical properties are independent of direction, the Zener anisotropy factor takes the value of 1, whereas when a value of A is smaller or greater than unity, it indicates elastic anisotropy.[39] For cubic systems, the universal Zener anisotropy factor is expressed as

$$A = \frac{2C_{44}}{C_{11} - C_{12}} \tag{7}$$

Zener anisotropy factor value of 1.789 (3.050) obtained when PBEsol (PBE) functional is used, vary from unity ($A \neq 1$) indicating that the quaternary compound under study possess mechanical anisotropy, implying its mechanical properties are

dependent on direction (axis) in which stress or strain is applied. The elastic anisotropy of a material is related to the abnormal growth of crystal grains, transformation, and formation of material structure and ability to induce micro-cracks in a material which has important implication in design engineering.[40]

To get a deeper view on the elastic anisotropy of cubic Rb_2LiTlF_6, the directional dependence of shear and Young's modulus in units of GPa are provided in **Figure 3**a,b. The curved surface plots in three dimensionality (3D) elucidate that this compound is elastically anisotropic due to non-uniform appearance when subjected to stress or strain along the x, y, and z axis. For elastically isotropic compounds the surface appears spherical but not curved.

Equation (8) was used to compute the value of Poisson's ratio from the values of bulk and shear modulus obtained, where a value of 0.30 (0.32) of Poisson's ratio was attained for PBEsol (PBE), confirming that the magnitude of longitudinal strain exceeds the transverse strain in this ternary compound.

$$\nu = \frac{1}{2}\left[\frac{B - \frac{2}{3}G}{B + \frac{1}{3}G}\right] \tag{8}$$

Kleinman parameter (ζ) describes the relative positions of the cation and anion sublattices under volume conserving strain distortions for which positions are not fixed by symmetry. For cubic systems, the Kleinman parameter can be computed from the values of two independent elastic coefficients as[41]

$$\zeta = \frac{C_{11} + 8C_{12}}{7C_{11} + 2C_{12}} \tag{9}$$

The Kleinman parameter describes the ease of bond bending to the bond stretching in cubic materials, whereby minimizing the bond bending leads to $\zeta = 0$, and minimizing the bond stretching leads to $\zeta = 1$. Thus, since our computed value is 0.665 (0.770) for PBEsol (PBE), we opine that one can easily minimize bond stretch in this material relative to bond bending. Additionally, with an idea of the magnitude of elastic coefficient C_{11} that indicates the resistance of a material to linear compression along the x-axis, we computed our predicted value of melting temperature of cubic Rb_2LiTlF_6 using both functionals as given in **Table 3** by applying empirical expression given by Equation (10)[42]

$$T_m = [553K + (5.9K/GPa)C_{11}] \pm 300K \tag{10}$$

The propagation velocity of longitudinal and transverse waves along different crystal directions is related to the elastic constants based on Navier's equation[43] as provided in Equation (11) that were applied in computing the predicted values of transverse, longitudinal, and average sound velocities given in Table 2. A longitudinal wave arises when atoms move in the direction of wave propagation whereas transverse waves occur when atoms move perpendicularly to the direction of wave propagation. The velocity parameters are
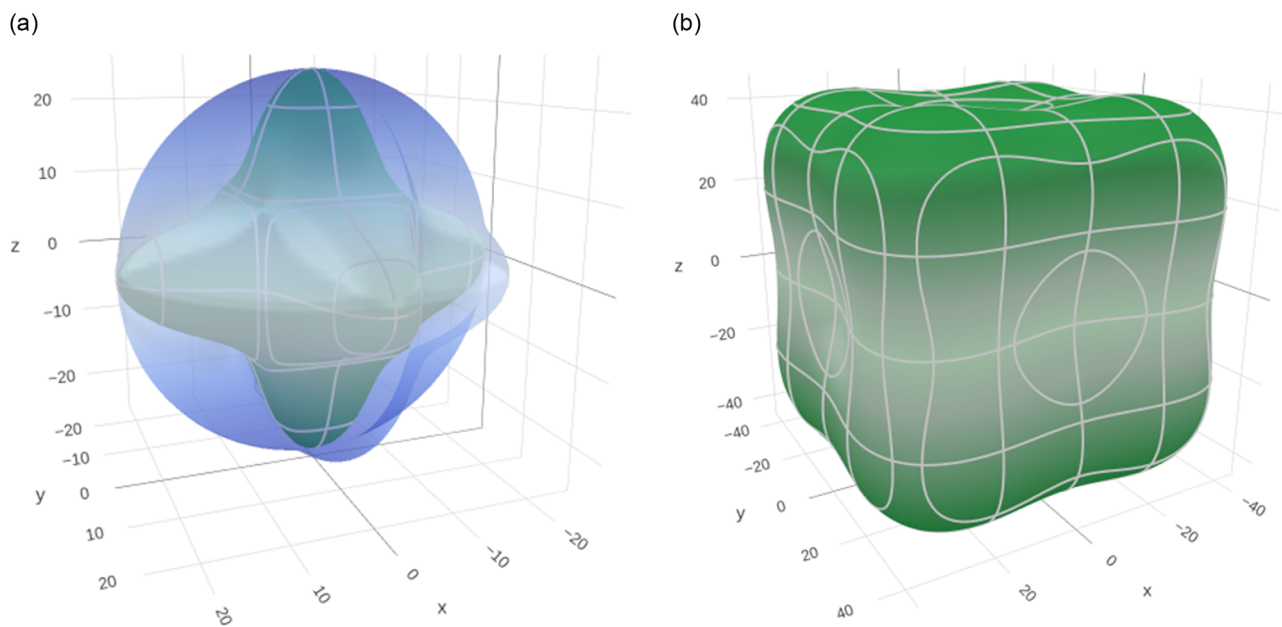
Figure 3. a) 3D plot of shear modulus, showing elastic anisotropy when forces are exerted on x-, y-, and z-axes; b) 3D plot of Young's modulus, showing elastic anisotropy when forces are exerted on x-, y-, and z-axes.

Table 3. Additional mechanical parameters and sound velocities of cubic Rb$_2$LiTlF$_6$ perovskite whereby ζ, a, Θ_D, T_m, ν_t, ν_l, and ν_m denote Kleinman parameter, Zener anisotropy factor, Debye temperature, melting temperature, tranverse, longitudinal, and average sound velocity, respectively.

	ζ	A	Θ_D [K]	T_m [K]	ν_t [m s^{-1}]	ν_l [m s^{-1}]	ν_m [m s^{-1}]
Calc. (PBE)	0.770	3.050	267.18	829.83	1709.46	3351.05	2279.36
Calc. (PBEsol)	0.665	1.789	300.39	909.64	1902.34	3569.26	2512.09

$$\nu_l = \sqrt{\frac{1}{3\rho}[3B+4G]}; \quad \nu_t = \sqrt{\frac{G}{\rho}}; \quad \nu_m = \left[\frac{1}{3}\left(\frac{2}{\nu_t^3}+\frac{1}{\nu_l^3}\right)\right]^{-1/3};$$

$$\Theta_D = \frac{h}{k_B}\left[\frac{3n}{4\pi}\left(\frac{N_A\rho}{M}\right)\right]^{1/3}\nu_m \tag{11}$$

By examining the tabulated values of ν_l and ν_t provided in Table 3, sound travels faster in the longitudinal direction than in the transverse mode of this cubic perovskite. From our data, we speculate that within a second, sound energy will propagate over an averaged distance of about 2512 m in this material from our PBEsol findings.

Thermal properties of a material are related to Debye temperature (Θ_D) as indicated in Equation (11), where k_B is the Boltzmann constant, h is the Plank constant, n is the number of atoms in its chemical formula, N_A is the Avogadro constant, ρ is the density of the material, and M is the molecular weight. Upon filling-in the values of entities of our material onto Θ_D formula provided, we extracted its Debye temperature to be 300.39 K (267.18 K) from PBEsol (PBE) functional data as listed in Table 3. Recall that Debye temperature is used to assess the

temperature above which all modes begin to be excited and below which modes begin to be frozen out.[44]

3.3. Electronic Band Structure, Partial, and Total Density of States

The electronic band structure provided in **Figure 4**a indicates that this double perovskite material has a direct band gap at the Γ-point in the Brillouin zone, hence we expect the nature of optical transition in cubic Rb$_2$LiTlF$_6$ to be direct transition, which is beneficial in solar cell applications since the band gap directly controls optical properties like the onset of photon absorption. The magnitudes of the computed direct electronic band gap of the double perovskite of interest are tabulated in **Table 4** as obtained using the stated techniques that have varying degree of approximation.

Figure 4b shows the partial (elemental) as well as the total density of states. It is visible that the states of fluorine dominates the top of the valence band. Both thallium and fluorine states are also noticeable at the bottom of the conduction band. Rubidium states appear far from the Fermi level (reference point) mainly between −8 and −6 eV, whereas contributions from lithium is neglegible within the presented energy range.

3.4. Phonon Dispersion and Thermal Properties of Rb$_2$LiTlF$_6$

The cubic Rb$_2$LiTlF$_6$ exhibits phonon dispersion with only positive frequencies (hard modes) throughout the Brillouin zone indicating its thermodynamically stability as revealed in **Figure 5**a. Below the acoustic cut-off frequency which is about 2.1 THz for this material, the acoustic phonon modes are present and above this frequency the optical phonon modes exist. From the plot of partial and total phonon density of states provided in
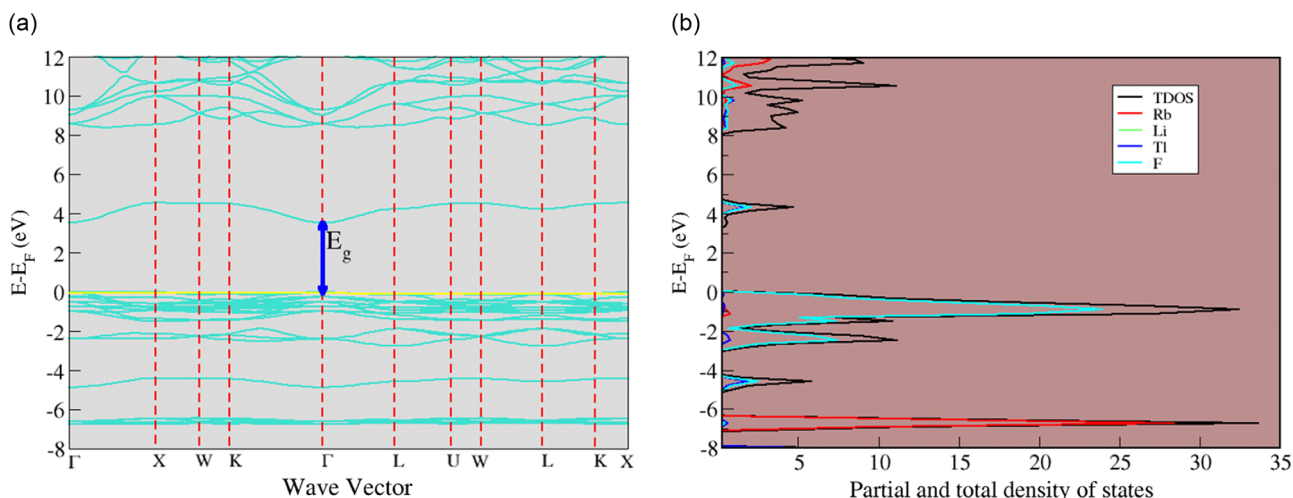
Figure 4. a) Electronic band structure, indicating the nature of the transition and the magnitude of the band gap, as obtained from PBEsol functional when the Fermi-energy is referenced to zero; b) Total and partial density of states from PBEsol, showing elemental composition of states when the Fermi-energy is referenced to zero.

Table 4. Electronic band gaps from our various approaches along with other theoretical work. Note that there is no experimental values of the gaps reported at the moment.

Approach	Others (PBE)[20]	Calc. (PBEsol)	Calc. (mBJ)	Calc. (HSE06)
E_g [eV]	3.47	3.51	5.50	5.57

Figure 5a, rubidium atoms are the main contributor to the acoustic phonon vibrations whereas lithium contributes the least to the acoustic phonon modes. As the lattice vibrate, it generates mechanical waves that carry heat and sound through the material. Above 8 THz frequency which is the upper part of the optical phonon region, the contribution from fluorine and lithium outweighs the other two.
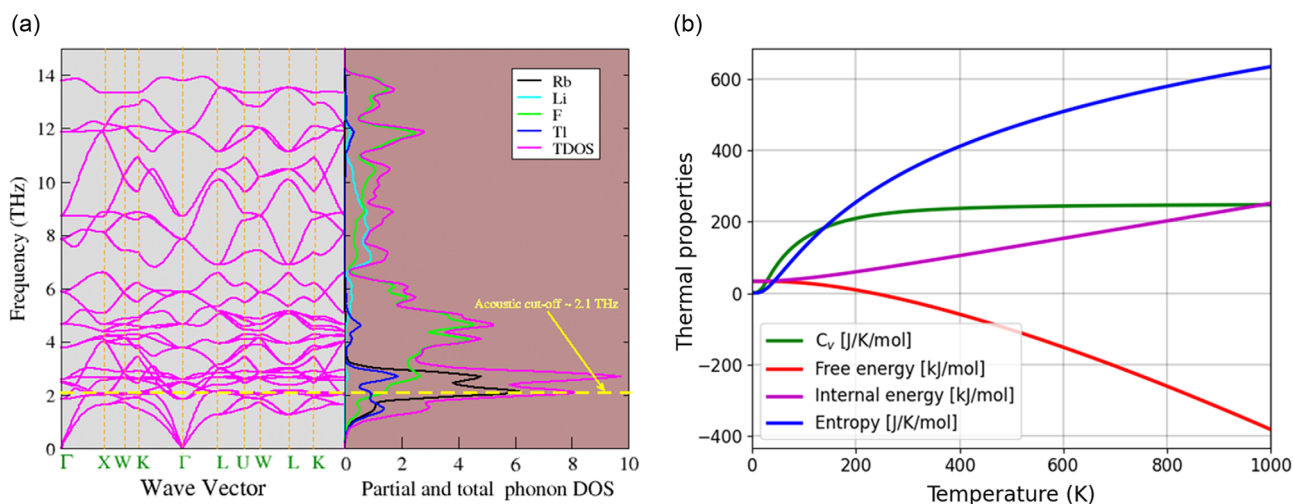
The predicted values of specific heat capacity, Helmholtz free energy, internal energy, and entropy at room temperature (300 K) were obtained to be 228.95 J (mol K)$^{-1}$, -21.60 kJ mol^{-1}, 81.52 kJ mol^{-1}, and 343.72 J (mol K)$^{-1}$, respectively as shown in Figure 5b. It is evident that the degree of disorderness (entropy), increases with an increase in temperature whereas the reverse is true for the Helmholtz free energy. In contrast, specific heat capacity increases with an increase in temperature and attains saturation point as temperature rises further. At a value of 242 J (mol K)$^{-1}$, specific heat capacity of cubic double perovskites type Rb$_2$LiTlF$_6$ approaches the Dulong–Petit limit. The Helmholtz free energy is an important parameter in determining the stability of a structure. A structure with more negative value of Helmholtz free energy is considered stable,[45] our predicted value of -21.60 kJ mol^{-1} reinforces our material's stability.

Figure 5. a) Phonon dispersion relation, indicating vibrational stability. Magenta lines on the left represents the phonon bands whereas black, cyan, green, and blue lines on the right indicates contributions from Rb, Li, F, and Tl, respectively; b) Specific heat capacity, entropy, internal, and free energy as a function of temperature as indicated by green, blue, magenta, and red lines, respectively.

Additionally, the internal energy at 0 K is attributed to the existence of zero point motion, the calculated values of internal energy and Helmholtz free energy at absolute zero temperature is 33.14 kJ mol^{-1} as shown in Figure 5b.

3.5. Thermophysical Properties of Rb$_2$LiTlF$_6$ Under Quasi-Harmonic Approximation

The quasi-harmonic approximation (QHA) that is implemented in phonopy[25] was used to predict the behavior of thermophysical properties of our compound of interest. Thermal properties at constant temperature ($P = 0$) were calculated at 11 volume points and the resultant thermodynamic functions were then fitted to the integral form of the Vinet EOS. The energy-volume optimization data was used as input to determine the thermophysical properties of our material.

In the plot showing volume dependence of free energy, the blue circles denote the free energy values calculated for a given volume points at every 100 K between 0 and 900 K. The minimum values of free energy at various volumes are depicted by the red dots. From the thermal expansion data, the value of thermal expansion coefficient at a temperature 300 K, was obtained to be 3.486×10^{-5} K^{-1}. We also used our predicted value of melting temperature computed using PBEsol functional (909.64 K, provided in Table 3) together with Equation (12), to approximate the coefficient of thermal expansion for this material from the inverse proportionality relation between the thermal expansion coefficient and melting point.[46]

$$\alpha = \left[\frac{0.038}{T_m} - 7.0 \times 10^{-6} \right] K^{-1} \qquad (12)$$

This resulted in a value of 3.478×10^{-5} K^{-1}, which is in accord with that obtained from the QHA approach. The coefficient of thermal expansion relates the change in volume of a material as a function of temperature change under constant pressure. It indicates the extent to which a given material expands upon heating. In **Figure 6**b,c, there is a gradual increase in volume and thermal expansion coefficient as temperature rises. There is no sudden change or anomaly seen within the considered temperature regime, which indicates the compound under study is thermally stable.

3.6. Optical Properties of Rb$_2$LiTlF$_6$

For us to understand the opto-electronic properties of Rb$_2$LiTlF$_6$, optical calculations were carried out using a four step procedure. Firstly, the converged HSE06 orbitals were determined for a few unoccupied orbitals followed by exact diagonalization, where a large number of unoccupied orbitals were used. At this point, the derivative of the orbitals with respect to the wave vector **k** (waveder) were obtained and used to construct the head and wings of the dielectric matrix. At the third step, the GW$_o$ calculation was done in which the quasi-particle eigen-values were updated iteratively, recall that GW$_o$ calculations provides the electronic band gap whereas the optical band gap is obtained by solving the Bethe–Salpeter equations to obtain the oscillator strength, which was the forth step in our procedure.

After obtaining dielectric matrix of the double perovskite type Rb$_2$LiTlF$_6$ at BSE level, we derived its optical features such as absorption $\alpha(\omega)$, refractive index $n(\omega)$, extinction coefficient $k(\omega)$, and reflectivity $R(\omega)$, as functions of photon energy (ω) from real $\varepsilon_1(\omega)$ and imaginary part $\varepsilon_2(\omega)$ of the dielectric function as per the Krammer–Kronig relations[47,48] provided in Equation (13) and (14)

$$\alpha(\omega) = \sqrt{2} \left[\sqrt{\varepsilon_1^2(w) + \varepsilon_2^2(w)} - \varepsilon_1(w) \right]^{\frac{1}{2}};$$

$$n(\omega) = \frac{1}{\sqrt{2}} \left[\sqrt{\varepsilon_1^2(w) + \varepsilon_2^2(w)} + \varepsilon_1(w) \right]^{\frac{1}{2}} \qquad (13)$$
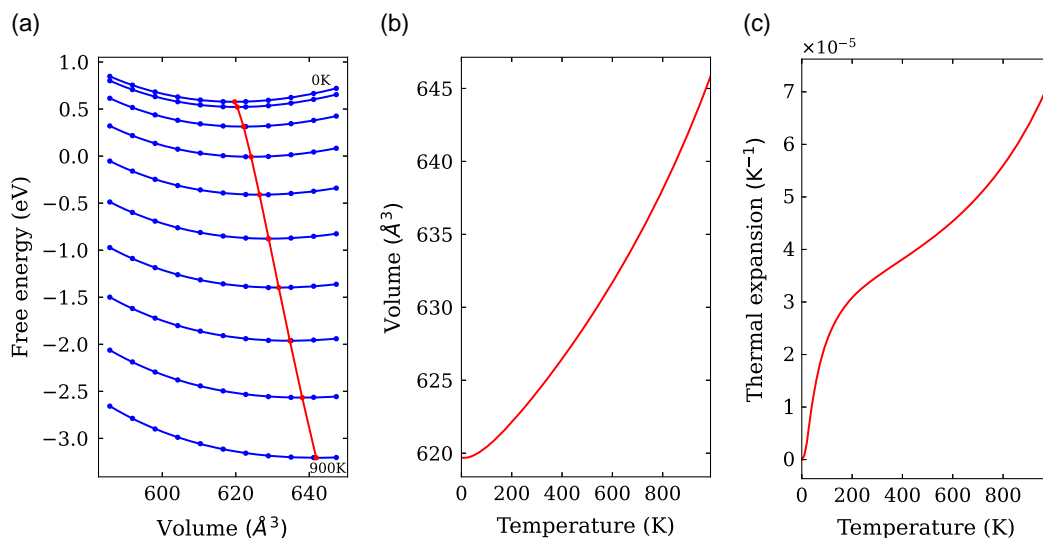

Figure 6. Figure 6a shows the variation of free energy with respect to volume, whereas temperature dependence of volume and thermal expansion are depicted in Figure 6b,c, respectively.

$$k^2(\omega) = \frac{1}{2}\left[\sqrt{\varepsilon_1^2(w) + \varepsilon_2^2(w)} - \varepsilon_1(w)\right];$$

$$R(\omega) = \left|\frac{\sqrt{\varepsilon_1(w) + j\varepsilon_2(w)} - 1}{\sqrt{\varepsilon_1(w) + j\varepsilon_2(w)} + 1}\right| \quad (14)$$

from our findings, the real and imaginary parts of the dielectric constant of this material show a minute degree of optical anisotropy in the x, y, and z axes depending on the point of light incidence. This is supported by the optical anisotropy plot and directional dependent values of real part and imaginary part of dielectric constant provided in the supporting information (provided in the github repository). Hence, for simplicity, we present optical properties obtained using averaged values of the optical data within a photon energy range of 12 eV. **Figure 7**a shows the real and imaginary parts of the dielectric function with respect to energy. The static dielectric constant $\varepsilon_2(0)$ is given by the low energy limit of $\varepsilon_1(\omega)$ and the computed value of static dielectric constant of our material is 1.2. Upon substituting the values of $\varepsilon_1(\omega)$ and $\varepsilon_2(\omega)$ onto Equation (13) and (14), other optical characterization parameters such as α, n, k, and R were obtained so as to critically examine the light dispersion behavior of the optical constants.

In Figure 7b, we present the absorption coefficient of the material under study as a function of photon energy. The inset plot indicates that the optical gap of the material was obtained to be 4.1 eV as determined from the plot of absorption coefficient via extrapolating the linear region of the onset of absorption (as indicated in the dotted line). The absorption coefficient determines the distance at which light of a particular energy or wavelength can penetrate a given material before it is absorbed.

Figure 8 shows the refractive index and extinction coefficient as a function of photon energy. The static values of refractive index and the extinction coefficient were obtained to be 1.1 and 0.78, respectively. The refractive index of a material is the ratio of speed of light in vacuum to its speed in the material under study. It indicates the degree of bending of the electromagnetic radiation as it transits between two different media. The low

value of static refractive index suggests that this material can be used in optical coating.

In contrast, extinction coefficient is given by the sum of scattering and absorption of the electromagnetic waves going through the material. From Figure 8b, the static value of reflectivity was obtained to be 0.12 and the highest value of reflectivity is attained when the energy of the incoming photons is about 7.9 eV. At this energy value, approximately 29% of the incoming solar radiation is reflected. This is also the energy value in which the imaginary part of the dielectric constant shows a steep peak and occurs at the point where the real part of the dielectric function becomes negative as depicted in Figure 7a.

The appearance of multiple absorption peaks within the range of 4–6 eV as shown in Figure 7b reveals multiple electronic transition probability from the valence to the conduction band. Note that there is no reported work on optical properties of this compound so far. Our predicted value of optical gap of cubic Rb_2LiTlF_6 was obtained to be 4.1 eV, which falls in the ultraviolet (UV) part that is outside the visible region of the electromagnetic spectrum. Therefore, we can classify this quaternary double perovskite as a wide band gap semiconductor, which can be applied in tandem configuration of solar cells, where it can be utilized as top-cell to efficiently absorb high-energy photon, hence increasing the overall spectral absorption range of the tandem device.

Principally, materials with band gaps outside the visible range of the electromagnetic spectrum are used in solar cells to harness the energy from UV and infrared light. These materials are used in combination with other materials that absorb visible light to create tandem solar cells that can convert a wider range of the solar spectrum into electrical energy[49] because a semiconductor with a particular band gap can absorb only those photons with energies higher than its band gap. However, the excess energy from photons with a higher energy than the band gap is lost through a thermalization process, in which the excited electrons relax to the conduction band edge.

In this regard, we suggest that Rb_2LiTlF_6 can be considered as a top-cell in tandem configuration of solar cells. The wide band

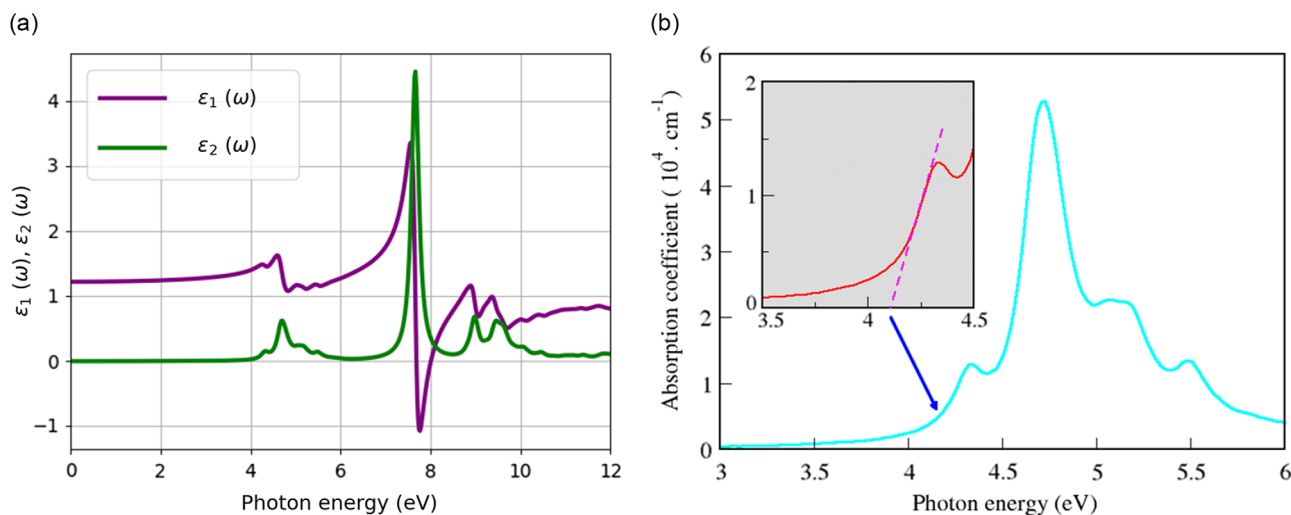**Figure 7.** a) Real (ε_1) and imaginary (ε_2) parts of the dielectric function with respect to photon energy. Static values of ε_1 and ε_2 are obtained when photon energy is zero. b) Absorption coefficient (α) as a function of photon energy. The inset plot (grey) indicates how the optical gap was determined.
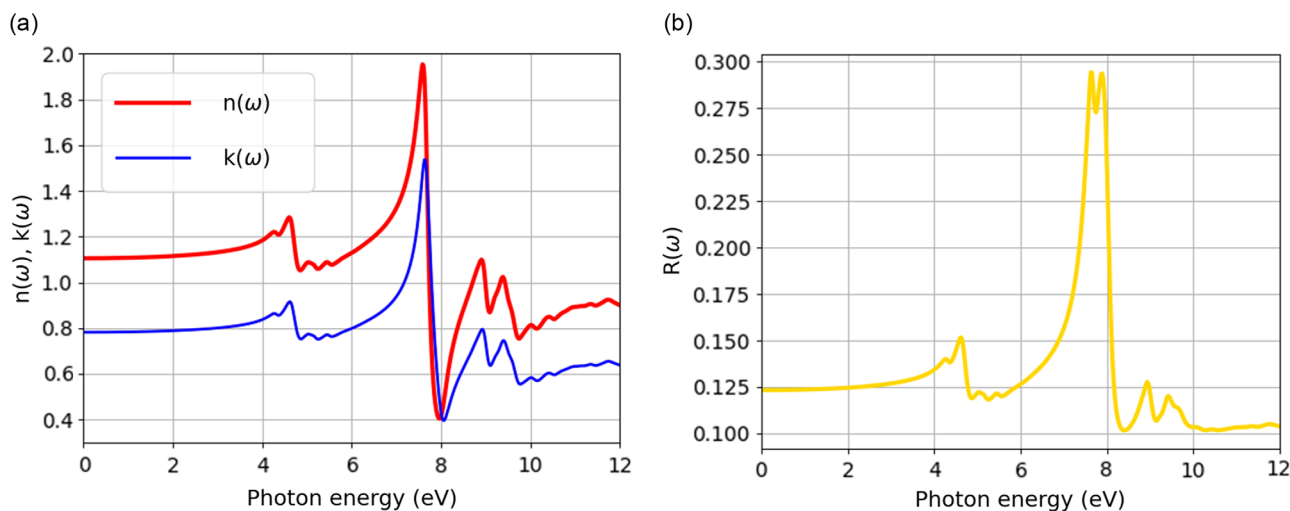
Figure 8. a) Refractive index (*n*) and exctinction coefficient (*k* as a function of photon energy. Static values of *n* and *k* are obtained when photon energy is zero. b) Reflectivity (*R*) as a function of photon energy. The maximum reflectivity is visible at about 7.9 eV photon energy value.

gap is itself an important advantage for photodetectors, since it enables room-temperature operation providing intrinsic visible-blindness. By virtue of being envisioned to be a wide band gap semiconductor, this material is rich in untapped potential that can be used to fabricate UV detectors that are helpful in military applications, flame detection, optical communications, emitter calibration, air purification, ozone hole monitoring, leak detection, and astronomical studies among others.[50,51] From the predicted optical band gap value of 4.1 eV, we opine that this material has potential in development of Rb_2LiTlF_6-based UV B LED with a peak wavelength value of about 302 nm for applications such as solid state lighting and anti-microbial lamps for UV B light microbial inactivation.[52]

4. Summary and Conclusion

The main goal of this study was to explore and understand through DFT approach the fascinating properties of Rb_2LiTlF_6, ranging from how its crystals are structured to its response when stress is applied as well as its behavior when illuminated with sunlight, so as to get insights of its fundamental physical properties and possibly obtain a glimpse of its anticipated applications. From our findings, Rb_2LiTlF_6 is expected to crystallize in an fcc structure. It is energetically stable based on the negative values of both the cohesive and formation energies obtained. Its phonon dispersion relation attest that it is dynamically stable due to absence of soft modes in the Brillouin zone. Goldschmidt tolerance factor was obtained to be 0.97, indicating the A-site cation has the appropriate size to fit in the interstices affirming its structural stability. Upon examining its mechanical data as per the laid down guidelines, we conclude that this double perovskite is mechanically stable and is ductile in nature. Additionally, it possess elastic anisotropy since its mechanical features are directionally dependent.

Besides being considered as the top-cell in tandem photovoltaics (solar cells with multiple layers), wide band gap semiconductors have myriad applications such as photodetection and scintillation, where materials with band gaps outside the visible range are used to detect radiations in the infrared and ultraviolet regions of the electromagnetic spectrum. They can also be used to create or design light emitting diodes that emit light in the ultraviolet regime, which is useful in sensing, communication, and medical technology. Since there is inadequate literature available about this material, this work may serve as a basic guide that will not only inspire but also catalyze future scientific work on cubic Rb_2LiTlF_6 and other related double perovskites that are yet to be synthesized and discovered from experimental and theoretical communities respectively, so as to validate, tailor, and even enhance the advancement of various exciting properties predicted through our computation with a diversified futuristic practical applications.

Conflict of Interest

The authors declare no conflict of interest.

Author Contributions

All authors participated in conceptualization, review, and editing. E.K.R., a postdoctoral fellow, performed all the calculations, analyzed the reported

data and wrote the manuscript under project supervision of N.E.M. and co-supervision of R.R.M., R.E.M., and J.K.K.

[1] T. Saha-Dasgupta, *Mater. Res. Express* **2020**, *7*, 014003.
[2] H. Kim, C. Lee, J. Im, K. Lee, T. Moehl, A. Marchioro, S. Moon, R. Humphry-Baker, J. Yum, J. Moser, *Sci. Rep.* **2012**, *2*, 591.
[3] S. Stranks, G. Eperon, G. Grancini, C. Menelaou, M. Alcoder, T. Leijtens, L. Herz, A. Petrozza, H. Snaith, *Science* **2013**, *342*, 341.
[4] A. Buin, P. Pietsch, J. Xu, O. Voznyy, A. Ip, R. Comin, E. Sargent, *Nano Lett.* **2014**, *14*, 6281.
[5] M. Grätzel, *Nat. Mater.* **2014**, *13*, 838.
[6] G. Niu, X. Guo, L. Wang, *J. Mater. Chem. A* **2015**, *3*, 8970.
[7] G. Divitini, S. Cacovich, F. Matteocci, L. Cinà, A. Di, C. Ducati, *Nat. Energy* **2016**, *1*, 1.
[8] C. Stoumpos, C. Malliakas, M. Kanatzidis, *Inorg. Chem.* **2013**, *52*, 9019.
[9] N. Wolf, B. Connor, A. Slavney, H. Karunadasa, *Angew. Chem.* **2021**, *133*, 16400.
[10] G. Meyer, *Prog. Solid State Chem.* **1982**, *14*, 141.
[11] S. Vasala, M. Karppinen, *Prog. Solid State Chem.* **2015**, *43*, 1.
[12] A. Slavney, T. Hu, A. Lindenberg, H. Karunadasa, *J. Am. Chem. Soc.* **2016**, *138*, 2138.
[13] G. Volonakis, A. Haghighirad, R. Milot, W. Sio, M. Filip, B. Wenger, M. Johnston, L. Herz, H. Snaith, F. Giustino, *J. Phys. Chem. Lett.* **2017**, *8*, 772.
[14] A. Slavney, L. Leppert, V. Saldivar, D. Bartesaghi, T. Savenije, J. Neaton, H. Karunadasa, *Angew. Chem.* **2018**, *130*, 12947.
[15] T. Tran, J. Panella, J. Chamorro, J. Morey, T. McQueen, *Mater. Horiz.* **2017**, *4*, 688.
[16] Z. Wu, K. Yi, Q. Tang, J. Gu, X. Zhu, *J. Alloys Compd.* **2023**, *930*, 167431.
[17] Y. Xiang, Z. Liu, Y. Gao, L. Feng, T. Zhou, M. Liu, Y. Zhao, X. Lai, J. Bi, D. Gao, *Chem. Eng. J.* **2023**, *456*, 140901.
[18] M. Hossain, D. Samajdar, R. Das, A. Arnab, M. Rahman, M. Rubel, M. Islam, H. Bencheif, R. Pandey, J. Madan, *Energy Fuels* **2023**, *37*, 3957.
[19] M. Manzoor, M. Iqbal, M. Imran, A. Mahmood, Y. Alanazi, S. Aftab, *J. Mater. Res. Technol.* **2022**, *18*, 4775.
[20] The Materials Data Project, *Double Perovskite Halide Compounds* **2018**.
[21] J. Hafner, *J. Comput. Chem.* **2008**, *29*, 2044.
[22] P. Hohenberg, W. Kohn, *Phys. Rev.* **1964**, *136*, B864.
[23] J. Perdew, K. Burke, M. Ernzerhof, *Phys. Rev. Lett.* **1996**, *77*, 3865.
[24] J. Perdew, A. Ruzsinszky, G. Csonka, O. Vydrov, G. Scuseria, L. Constantin, X. Zhou, K. Burke, *Phys. Rev. Lett.* **2008**, *100*, 136406.
[25] A. Togo, I. Tanaka, *Scr. Mater.* **2015**, *108*, 1.
[26] R. Gaillac, P. Pullumbi, F. Coudert, *J. Phys.: Condens. Matter* **2016**, *28*, 275201.
[27] J. Perdew, M. Levy, *Phys. Rev. Lett.* **1983**, *51*, 1884.
[28] R. Ahmed, S. Hashemifar, H. Akbarzadeh, M. Ahmed, *Comput. Mater. Sci.* **2007**, *39*, 580.
[29] V. Goldschmidt, *Naturwissenschaften* **1926**, *14*, 477.
[30] J. Young, J. Rondinelli, *J. Phys. Chem. Lett.* **2016**, *7*, 918.
[31] J. Bechtel, A. Van der Ven, *Phys. Rev. Mater.* **2018**, *2*, 025401.
[32] K. Momma, F. Izumi, *J. Appl. crystallogr.* **2008**, *41*, 653.
[33] R. Hill, *Proc. Phys. Soc. London, Sect. A* **1952**, *65*, 349.
[34] F. Mouhat, F. Coudert, *Phys. Rev. B* **2014**, *90*, 224104.
[35] R. Yu, J. Zhu, H. Ye, *Comput. Phys. Commun.* **2010**, *181*, 671.
[36] S. Pugh XCII, *London, Edinburgh Dublin Philos. Mag. J. Sci.* **1954**, *45*, 823.
[37] J. Lewandowski, W. Wang, A. Greer, *Philos. Mag. Lett.* **2005**, *85*, 77.
[38] V. Kanchana, S. Ram, *Intermetallics* **2012**, *23*, 39.
[39] Z. Clarence, *Elasticity and Anelasticity of Metals*, University of Chicago Press, Chicago, IL **1948**.
[40] J. Zhang, Y. Zhang, K. Xu, *J. Cryst. Growth* **2005**, *285*, 427.
[41] E. Güler, M. Güler, *Mater. Res.* **2014**, *17*, 1268.
[42] C. Nianyi, L. Chonghe, Y. Shuwen, W. Xueye, *J. Alloys compd.* **1996**, *234*, 130.
[43] O. Anderson, *J. Phys. Chem. Solids* **1963**, *24*, 909.
[44] T. Nakashima, Y. Umakoshi, *Philos. Mag. Lett.* **1992**, *66*, 317.
[45] N. Aarifeen, A. Afaq, *Chin. Phys. B* **2017**, *26*, 093105.
[46] J. Bala, D. Singh, D. Pandey, C. Yadav, *Int. J. Thermophys.* **2020**, *41*, 1.
[47] V. Lucarini, J. Saarinen, K. Peiponen, E. Vartiainen, *Kramers-Kronig Relations in Optical Materials Research*, Vol. 110, Springer Science & Business Media **2005**.
[48] J. Sun, H. Wang, J. He, Y. Tian, *Phys. Rev. B* **2005**, *71*, 125132.
[49] G. Eperon, M. Hörantner, H. Snaith, *Nat. Rev. Chem.* **2017**, *1*, 0095.
[50] H. Chen, K. Liu, L. Hu, A. Al-Ghamdi, X. Fang, *Mater. Today* **2015**, *18*, 493.
[51] E. Monroy, F. Omnès, F. Calle, *Semicond. Sci. Technol.* **2003**, *18*, R33.
[52] L. Hinds, C. O'Donnell, M. Akter, B. Tiwari, *Innovative Food Sci. Emerg. Technol.* **2019**, *56*, 102153.